Virtual Pixels Printed with Acoustic Mist Imaging

Meng H. Lean

Xerox Corporation, Wilson Center for Research & Technology, Micro-Systems and Media Laboratory, Sleepy Hollow, New York

This article details a simulation effort from first principles to evaluate the feasibility of using ink aerosols in a direct marking technology based on the ElectroPrint concept. This technology, called Acoustic Mist Imaging (AMI), uses acoustic or other nebulizer mechanisms to create a fine mist of droplets, which are then charged and directed onto a print medium to record the image. Drop charging is modeled using two approximations: a very rapid ballistic impact scheme; and by tracking individual ion trajectories with a more compute intensive self-consistent drift attachment model. Charged drops are then individually tracked to deposit on a print medium, producing virtual pixels. Results are generated for square and circular apertures at 600 spi, and for combinations of stationary and moving aperture-print media configurations to quantify image smearing. Preliminary data indicates that the technology is capable of 600 spi and higher print resolutions. Even higher resolution is achievable by synchronizing the velocities of both the print aperture and print medium, and by electrostatic focusing of the ion beam. Numerical experiments to duplicate the ElectroPrint images indicate that image smearing can be significantly reduced through a combination of uniform airflow velocity profile (slug flow) and increasing the deposition electric field.

Introduction

Acoustic Mist Imaging (AMI) is a direct marking concept derived from the ElectroPrint[1] technology, which was a product (EP-100) in the early 1970s. Its market niche was to serve as a line printer[2] for computer centers to produce high-speed draft quality (96 spi) printouts on fan-fold paper. With advent in technology on many fronts in the last three decades, the present motivation for AMI is to assess the feasibility of upgrading the technology to produce the 600 spi print resolution required for the contemporary market. Because little is known of the hardware implementation of the EP-100, simulation was therefore a logical alternative to attain three objectives: identify the critical parameters, optimize the interplay of the coupled physics, and determine a working parameter set to guide any hardware implementation.

In this modeling work, we identify the four key subsystems: mist generation, mist entrainment, mist charging, and mist deposition. From the literature,[3] it was established that mist generation is hardware dependent and can be de-coupled from this preliminary simulation aimed at demonstrating feasibility. Nebulizer and atomization technologies are varied for the gamut of ink viscosity, droplet sizes and distributions. Therefore, in

this work we assume that nominal 5 µm droplets can be generated in a controlled fashion using some established mechanism. Mist entrainment refers to drag acceleration of the droplets of some given density, which cause them to be advected within a laminar flow field as they enter the charging stage. Because the mist droplets are initially uncharged, we may assume little or no interaction between adjacent neighbors provided the number density is below some threshold limit of say a few percent by volume. This assumption simplifies the mist entrainment model to analytic considerations for initial conditions on time and distance to attain terminal velocity in a laminar flow field. The overall algorithm does indeed allow for drop to drop interactions.

Mist charging as depicted in Fig. 1 is much more complicated as it requires consideration of both ion and droplet trajectories and their interactions. The charge generation physics is not considered here although it has been modeled in some detail in prior work.[4] An ionographic head may be used for gating ions on demand into the print zone. Additional details are contained in the literature.[5] Therefore, the 3D particle model is developed for ion charging of mist droplets, which are randomly distributed beneath the aperture. Two charging models are developed and will be considered in more detail later in this article. Finally, mist deposition requires the trajectory tracking of charged droplets in some deposition E field and surrounding airflow, as shown in Fig. 2. Image smearing is an unknown of great concern and therefore requires the model to be precise in predicting individual drop deposition locations. The degree of dispersion is gauged by comparing the footprints of the virtual pixel and that of the deposited image.

Modeling Considerations

The primary purpose of this work is to demonstrate AMI feasibility. In the process, key subsystems pertain-
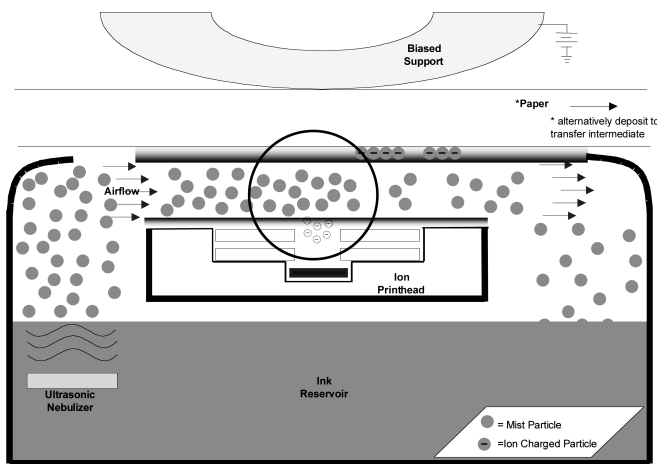
Figure 1. Illustration of mist/droplet charging and image deposition geometry. *Supplemental Materials can be found in color on the IS&T website (www.imaging.org) for a period of no less than 2 years from the date of publication.*

Figure 2. Three-dimensional illustration of single aperture charging and single pixel printing. The charging zone with the circular aperture is shown contiguous with the deposition zone. A bias voltage is applied to the upper electrode with the bottom electrode grounded. *Supplemental Materials can be found in color on the IS&T website (www.imaging.org) for a period of no less than 2 years from the date of publication.*

ing to charging and deposition are simulated in some detail. To make the problem size tractable, two contiguous computational cells are defined which represent the charging and deposition zones for a single aperture as shown in Fig. 2. Zero flux boundary conditions may be imposed on the vertical sides to simulate a situation when all the apertures are "ON". However, these conditions can also be relaxed to assess image cross talk, signified by the lateral spread of the charged drops across the walls of the cell. The computational cell for charging is a volume of 42.33 μm × 42.33 μm cross-section (600 spi) and 1 mm high (print gap). Within this volume are randomly distributed a finite number of drops corresponding to the specified number density. Two alternative schemes for drop charging simulation are used to compute the initial conditions for the drop deposition model. The computational cell for drop deposition is 42.33 μm by 15 mm in cross-section and 1 mm high. All image-forming drops are usually deposited within 15 mm from the point of charging at 10 ips airflow.

The models are developed with a great deal of generality to allow for wide coverage of the diverse scenarios that may need to be investigated in the quest for a working parameter set. For example, the models will accept empirical data on drop size distributions and randomly seed both ions and droplets to allow for statistical studies from a collection of runs to abstract subsystem behavior. Much simulation data can be accumulated relating to size and charge selectivity and other metrics used to gauge more traditional marking systems. The models can also be used to generate other virtual pixel prints for image quality analysis.

The complex models are fairly compute intensive and generate volumes of data to capture the dynamics of each simulation run. Through a combination of simulation approximations employing the theory of images, and implementation of approximate schemes for charge accumulation, both models involve quasi-analytic formulations, which enable them to execute very rapidly on both PCs and UNIX platforms. To facilitate rapid data analysis, the volumes of data from the simulations are displayed in several convenient forms. Interactive simulation and visualization on a UNIX platform uses *Xgraphix*, an X-window package from UC Berkeley. This feature allows very rapid visual correlation and diag-
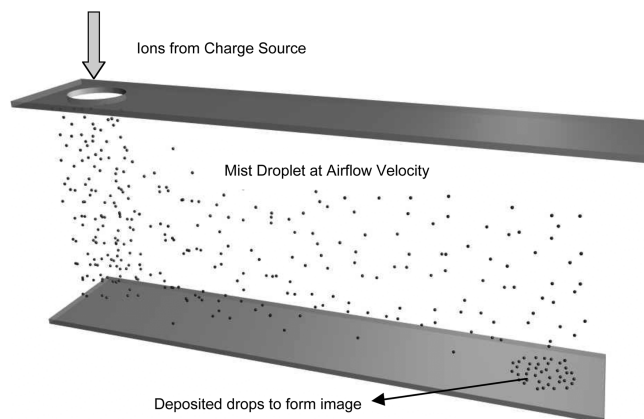
nosis of dynamic model performance and is particularly helpful in debugging new data sets. Presentation quality animations show replays of solution dynamics to facilitate understanding, and are prepared using *AVS* from Advanced Visual Systems.

Problem Formulation for Marking Subsystems

The mist entrainment, charging, and deposition subsystems are considered in more detail in the following discussion. Ion gating is briefly described in the literature.[6] Ballpark estimates of operating parameters are also abstracted from published literature.[7]

Mist Entrainment

Uncharged droplets generated by an ultrasonic nebulizer source may be introduced into a convective airflow as shown on the left of Fig. 1. These droplets are drag accelerated in the flow field according to the equation of motion:

$$m \, dv/dt = - \, 6\pi\eta r \, (v - U_o) \tag{1}$$

where v and U_o are the drop and airflow velocities, respectively. All other parameters are as defined in Table I. The time-dependent drop velocity is the solution in the process direction given by:

$$v(t) = U_o \, (1 - \exp(-t/\tau)) \quad \tau = m/6\pi\eta r \tag{2}$$

and τ is the acceleration time-constant. For the parameters under consideration, the 5 μm droplet is accelerated to 99% of its terminal velocity of 10 ips within 0.32 μs over a distance of 82 μm. These values indicate that the drag acceleration zone need only be a very compact extension just before the charging zone.

Mist Charging

Prior to charging, a finite number of droplets corresponding to the specified number density is randomly distributed immediately under the aperture using an algorithm that checks for and prevents geometrical overlap. This step is necessary to ensure a unique collection of non-contacting droplets. Next, the three time scales corresponding to the transit time of the ion, droplets, and charging pulse, are considered. For the parameters

Parameter	Description	Nominal Value
m	Drop mass	6.545×10^{-11} gm
r_{drop}	Drop radius	2.5 μm
ρ_{drop}	Ink density	1.0 gm/cm³
η	Air viscosity	2.0×10^{-5} kg/m.s
τ	Drag acceleration time constant ($m/6\pi\eta r_{drop}$)	69.4 μs
τ_{99}	Time to reach 99% of terminal velocity	0.3196 ms
d_{99}	Distance to accelerate to 99% of terminal velocity	81.35 μm

Parameter	Description	Nominal Value
s	Print resolution	600 spi
h	Pixel size	42.33 μm
g	Print gap	1 mm
μ	Ion mobility in air	2 cm²/V.s
E	Charging/Deposition E field	1 V/um
v_{ion}	Ion velocity (μE)	2×10^4 cm/s
t_{ion}	Ion transit time through gap (g/v_{ion})	5 μs
U_o	Airflow velocity	10 ips
$d_{aperture}$	Charging aperture diameter or side	30 μm
t_{drop}	Drop transit time through aperture ($d_{aperture}/U_o$)	0.1181 ms
t_{charge}	Charging time under aperture	2 μs
Δt	Time-step for 5 μm ($2r_{drop}$) displacement	25 ns
J	Charging current density	0.24 mA/cm²
I	Charging current ($\Delta Q/\Delta t$)	2.16 nA
ΔQ	Total image charge ($I\Delta t$)	4.32 fC
n_{ion}	Total number of ions ($\Delta Q/q$)	26,849
n_{drop}	Number of drops in computational cell at a density of 120,000/mm³	108

shown in Table II, the respective times are 5 μs, 0.1811 ms, and 2 μs. The ratio of ion to droplet velocity exceeds 787. This means that the droplets are quasi-static during the transit of ions through the print gap. Therefore, a first order approximation for droplet charging may involve the *ballistic impact* of ions on the immobile drops assuming negligible mutual repulsion of the ions during transit. Ions are also assumed to be fully captured by the drop on impact, with net charge accumulated at the drop centroid. This charging model works purely by geometric projection, and may result in clusters of drops near the aperture with much higher charge than those further below which are either blocked or not in the direct line of sight of the ions.

Another more precise approximation may be derived by allowing the ions to propagate among the essentially static droplets at very small time scales. Ions attach wherever they make contact with the drops. This *drift attachment* scheme uses the particle simulation algorithm, and will result in curvilinear ion trajectories. The ions are assumed to be massless so that collisions with neutrals are averaged over long time scales. The instantaneous ion velocities are then evaluated as:

$$\mathbf{v}_{ion} = \mu\mathbf{E} \qquad (3)$$

By arbitrarily requiring that the ions move a maximum distance of no more than the drop diameter, the resulting time-step is 25 ns. At 10 ips, the lateral distance moved by the drops in 2 μs is only 0.5 μm. Therefore an immediate simplification is to assume the drops are immobile during the charging step. These ions are injected into the print gap for the first 80 time-steps to correctly reflect the charging current density. This scheme may result in more uniform drop charging as those normally not in the initial line of sight of the ions may still be charged by a trickle down effect. All relevant parameters are calculated and displayed in Table II.

Mist Deposition
The deposition zone is assumed to be contiguous with the charging zone as the charged drops begin to migrate almost immediately with the applied bias field, as illustrated in Fig. 2. Using image symmetry, only one pixel width of the problem geometry needs to be modeled to reduce on overall problem size. The vertical sidewalls may be assumed to be zero flux boundaries. The charged droplets deposit to form the circular pixel produced by the circular aperture. The uncharged droplets proceed to move through the channel without depositing. The trajectories of these droplets are tracked *enmasse* together with the self-consistent E field solution. The algorithm is used in the same manner for the square aperture. This algorithm is similar to the drift attachment model previously used to simulate ion charging of droplets. All simulations are with respect to the Cartesian frame of reference shown in Fig. 2.

Numerical Implementation
Numerical implementation of the simulation models in both form and function require clear and unambiguous interpretations of the attendant physics, the assumptions and subsequent simplifications, and the validity and limitations of the generated results. More details on the particle simulation algorithm and related charging works are published in the literature.[8–11]

Particle Simulation Algorithm
The particle simulation algorithm is comprised of three sequential steps at every time interval:
- *Field Solve* – compute E fields by solving the Poisson equation:

$$\mathbf{E} = -\nabla\phi \qquad (4)$$

where potential, ϕ, and field $\mathbf{E}$ are given by:

$$\phi = q/4\pi\varepsilon_o r \quad \mathbf{E} = q/4\pi\varepsilon_o r^2\, \mathbf{a}_r \qquad (5)$$

The composite $\mathbf{E}$ field may include those due to other drop charge, polarization charge on dielectric interfaces, image symmetry, and deposition fields.
- *Particle Push* – compute accelerations and velocities by integrating the equation of motion:

$$m\, d\mathbf{V}/dt = q\mathbf{E} - 6\pi\eta r\, (\mathbf{V}-U_o(\mathbf{x})\mathbf{k}) - mg\,\mathbf{i} \qquad (6)$$

where parameters are as defined in Table II. In particular, the third term on the right is gravity, which is insignificant but is included here for completeness. Unit vectors, $\mathbf{i}$ and $\mathbf{k}$, are aligned in the X and Z directions, respectively. The step-wise computation for $(\mathbf{r},\mathbf{V})$ represents the integration of the Vlasov equations in phase space. The central difference scheme is used to track trajectories to second order:

$$\mathbf{r}(t+\Delta t) = 2\,\mathbf{r}(t) - \mathbf{r}(t-\Delta t) + [\mathbf{F}(t) - \mathbf{F}_{drag}]/m\Delta t^2$$

$$\mathbf{F}_{drag} = 6\pi\eta r\, dr/dt \qquad (7)$$

To first order, the airflow velocity profile is taken as a linear interpolation of the velocities on the top and bottom surfaces, representing the aperture and the print medium. Thus,

$$U_o(x) = U_{Print\ Medium} + x/g\ (U_{Aperture} - U_{Print\ Medium}) \quad (8)$$

- *Droplet Interactions* – check for mechanical interactions between drops and apply the necessary logic for moving them. In particular, contacting drops are made to coalesce with the new velocity obtained by conservation of linear momentum:

$$\mathbf{V}_{new} = m_1\mathbf{V}_1/(m_1 + m_2) + m_2\mathbf{V}_2/(m_1 + m_2) \quad (9)$$

The new drop size is obtained from summing the two volumes:

$$r_{new}^3 = r_1^3 + r_2^3 \quad (10)$$

and the new charge and mass is the summation of their individual charge and mass.

Field Solve Approximations

Particle simulations require discrete interactions and are therefore fairly compute intensive. For fully consistent simulations, the order of operations is N^2, where N is the number of particles. Provided N is not too large, problem size may be manageable. For really large N, a simplification is to use a particle–particle, particle-mesh scheme (P^3M) where field solve is performed over a grid of size M, where M << N. In this manner, problem size can be kept sufficiently tractable. This approximation is not needed here, as the number of particles is fairly small.

Input Parameters

The models require a set of independent input parameters that define the conditions for the run. These include: print resolution (spi); print gap (g); ion mobility (μ); deposition field (*E*); airflow velocity (U_o); aperture size ($r_{aperture}$); current density (*J*); and drop number density (n_{drop}). Other dependent parameters are inferred or derived from them. Nominal values tabulated in Table II are abstracted from the references and from discussions with colleagues. In particular, the level of charging current, *J*, is chosen to avoid cross talk between adjacent pixel streams. This is accomplished by iteratively adjusting the current level while relaxing the zero flux conditions on the sidewalls. The level of 0.24 mA/cm^2 obtained is when no charged drops cross the vertical sidewalls before they deposit onto the print medium. This level of current is pretty low by xerography standards, and will result in less image blooming in a direct marking configuration. As will be evident later, conditions that call for higher drop charge can also be met with a corresponding increase in deposition field.

Simulation Steps

Two models are developed to cater to both charging and deposition. The charging model handles the drift attachment simulation. The deposition model handles the drop deposition simulation. The ballistic impact charging model is implemented as an optional front-end. The drift attachment model data is accepted as input files from a pre-computation stage. The combined drop charging and deposition algorithm proceeds in the following sequence:

1. Specify input parameters
2. Generate random distribution of droplets in the charging cell
3. Generate random distributions of ions over a square region inscribing the circular or square apertures over the duration of the charging window (2 µs)
4. Perform *ballistic impact* or *drift attachment* computation of ion charging of drops
5. Process field solve, particle push, and mechanical interactions
6. Check for total drop deposition. If yes, exit. Else, if *t* < 2 µs, return to step 3 to continue charging. Otherwise, return to Step 5 to continue tracking.

Results and Discussion

Results are divided into four sets for discussion. In the first set, the relative performance of both drop charging models are compared. Virtual pixels are printed using circular and square apertures for comparison with the digital pixel to quantify smearing. The second set of results is generated with both aperture and print medium stationary to establish charge induced smearing. Next, results are generated for combinations of moving and stationary apertures and print medium to include drag-induced dispersion. Finally, operating conditions that may approximate those for the ElectroPrint EP-100 are simulated to study the mitigating effects of charging current, deposition field, and airflow profile on image dispersion.

Drop Charging

Figure 3 shows a snapshot of the *Xgraphix* interactive display of dynamic charging simulation for the circular aperture. The two top windows show distorted side views of attached ions on droplets and tracers of ions in transit. The computational cell geometry is 1 mm high and 50 µm × 50 µm in area. Consequently, the spherical droplets are compressed pancakes as seen from the side. The lower left window shows the top view of the ion distribution through a circular aperture. Tracers are ions in transit, voids are droplets on which ions have deposited. The lower right window shows the particle fractions for ions in air (ascending curve) and ions on droplets (descending curve). In Fig. 4(a) is shown a scatter plot of the accumulated charge on the randomly seeded drops as functions of their height in the gap using the ballistic impact charging model. As expected, drops with higher charge (on the right) are located closer to the aperture while lower charged drops are closer to the bottom electrode (on the left). There are quite a few uncharged drops in comparison with Fig. 4(b) computed using the drift attachment model. Both models predict up to 500 – 600 ion impacts/attachment resulting in a maximum drop charge accumulation of 0.08 fC. Another observation of note is that the scatter plot is more condensed vertically for the drift attachment model indicating that drop charge is relatively more uniform. Figure 5 shows a snapshot of the AVS animation for droplet charging with the drift attachment model through a square aperture. The red ion cloud charge blue droplets, and turn green on attachment to the droplets. A clear conclusion from these results is that at this low number density of 1%, both the ballistic impact and drift attachment models appear to predict fairly similar charging results. However, as can be seen in Table III, detailed statistics indicate some very interesting and intuitive observations. In particular, comparing data for the circular aperture, we note that:
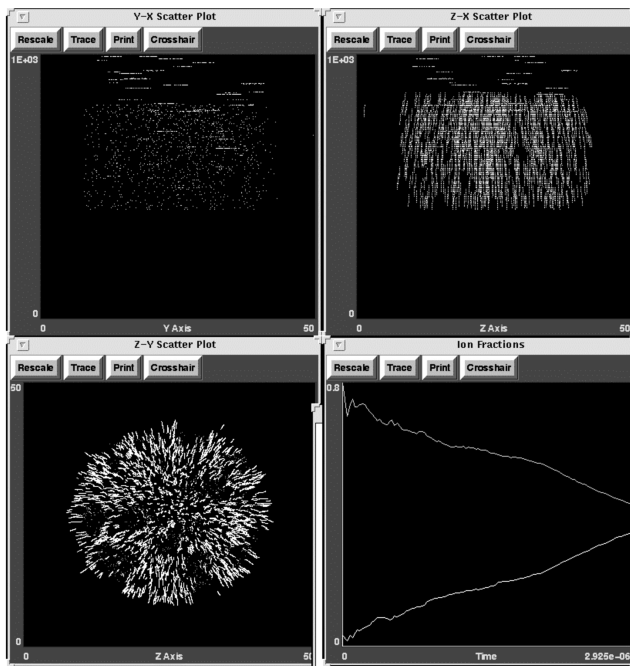
Figure 3. Snapshot of *Xgraphix* interactive display of dynamic charging simulation for circular charging aperture. The top left window shows a distorted side view of attached ions on droplets, and the ions in transit. The top right window shows the other side view with ion trajectories. The computational cell geometry is 1 mm high and 50 μm x 50 μm in area. Consequently, the spherical droplets are compressed pancakes as seen from the side. The lower left window shows the top view of the ion trajectories with voids being ions attached on droplets. The lower right window shows the particle fractions for ions in air and ions deposited on drops. *Supplemental Materials can be found in color on the IS&T website (www.imaging.org) for a period of no less than 2 years from the date of publication.*

- The drift attachment charging model predicts a lower percentage (54%) of charged drops compared to 71% for the ballistic impact model. This is because previously deposited ions on drops may repel subsequent incoming ions. As a result, the amount of ion lost to the lower ground electrode is 3x higher.
- The drift attachment charging model results in fewer uncharged drops (11%) compared to the ballistic impact model (18%). This is because the curvilinear ion trajectories are able to reach drops, which are otherwise outside the charging aperture or nested under the shadow of drops higher up in the gap and hence closer to the aperture.

Based on the preceeding, the expectation is that at higher densities, the preference is to use the drift attachment model.

Stationary Single Pixel Prints

This set of data, generated with both aperture and print medium stationary, attempts to separate air drag-induced image dispersion effects from consideration. Figures 6 and 7 are results for the circular aperture, and Fig. 8 is the corresponding result for the square aperture. Figure 6 shows a snapshot of the *Xgraphix* interactive display of dynamic droplet deposition simulation. Results are for stationary circular charging aperture and print medium using the drift attachment charging model. The top windows show side views of drop trajectories, which exhibit divergence due to mu-
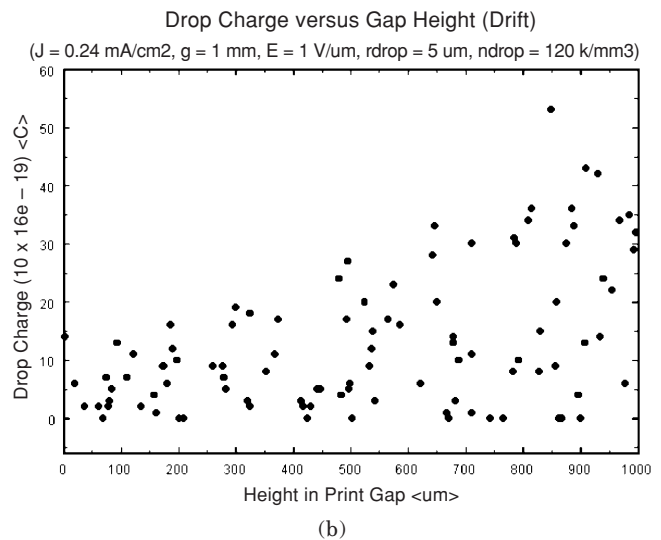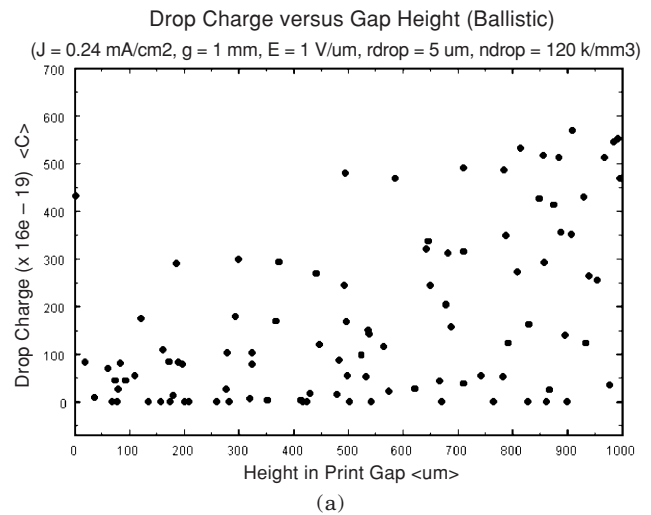

Figure 4. (a) Scatter plot of the accumulated charge on the randomly seeded drops as functions of their height in the gap using the ballistic impact charging model; (b) scatter plot of the accumulated charge on the randomly seeded drops as functions of their height in the gap using the drift attachment charging model. *Supplemental Materials can be found in color on the IS&T website (www.imaging.org) for a period of no less than 2 years from the date of publication.*

tual repulsion of ion charge. The lower left window shows the top view of the (yellow) ion trajectories through a circular aperture. The lower right window shows the particle fractions for drops (lower curve) in air and drops (upper curve) deposited on the print surface. In general, there is less beam deflection with the drift attachment model, resulting in a higher fraction of deposited drops within the same time frame. Figure 7(a) shows the virtual pixel print for the circular aperture with drops charged using the ballistic impact model. The original image is a 30 μm diameter circle outlined in blue. Smaller circles are outlines of deposited drops. Image dispersion of up to 5 μm is evident. Shown in Fig. 7(b) is the corresponding virtual pixel print using the drift attachment charging model. As can be seen, the results are fairly similar, probably due to the low number density. In Fig. 8, we see that the results for the square aperture follows a similar trend to what has been observed for the circular aperture case. The fraction of deposited drops is about 21% higher than for the
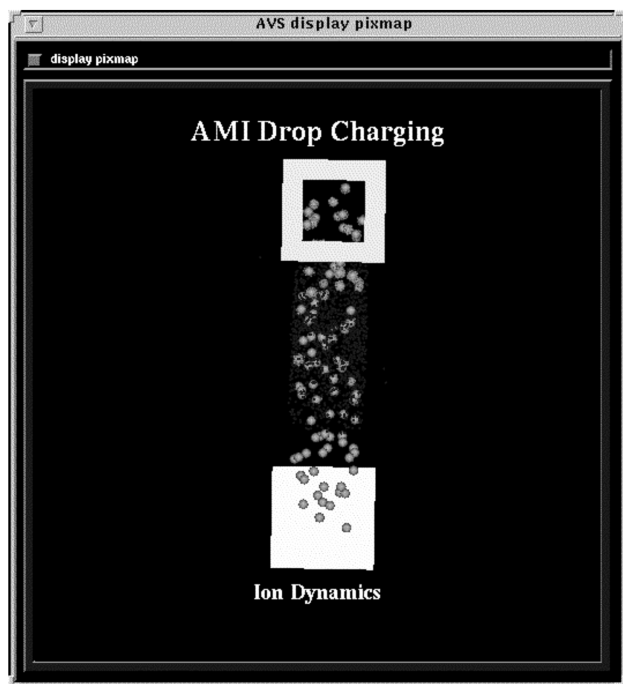
Figure 5. Snapshot of AVS animation of droplet charging through a square aperture. Red ions charge blue droplets, and turn green on attachment to the droplets. *Supplemental Materials can be found in color on the IS&T website (www.imaging.org) for a period of no less than 2 years from the date of publication.*

TABLE III. Model Predictions from Numerical Experiments

	Ballistic Charging Model			
Parameters	Circular Aperture		Square Aperture	
	r=15 μm		d=30 μm	
Ions on Drops	16940	70.58%	21022	87.59%
Ions on Aperture	5104	21.27%	0	0%
Ions on Collection Electrode	1956	8.15%	2978	12.41%
Total Ions	24000	100%	24000	100%
Uncharged Drops	18	18.0%	5	5.0%
Drops Outside Aperture	7	7.0%	0	0%
Charged Drops	75	75.0%	95	95.0%
Total Drops	100	100%	100	100%

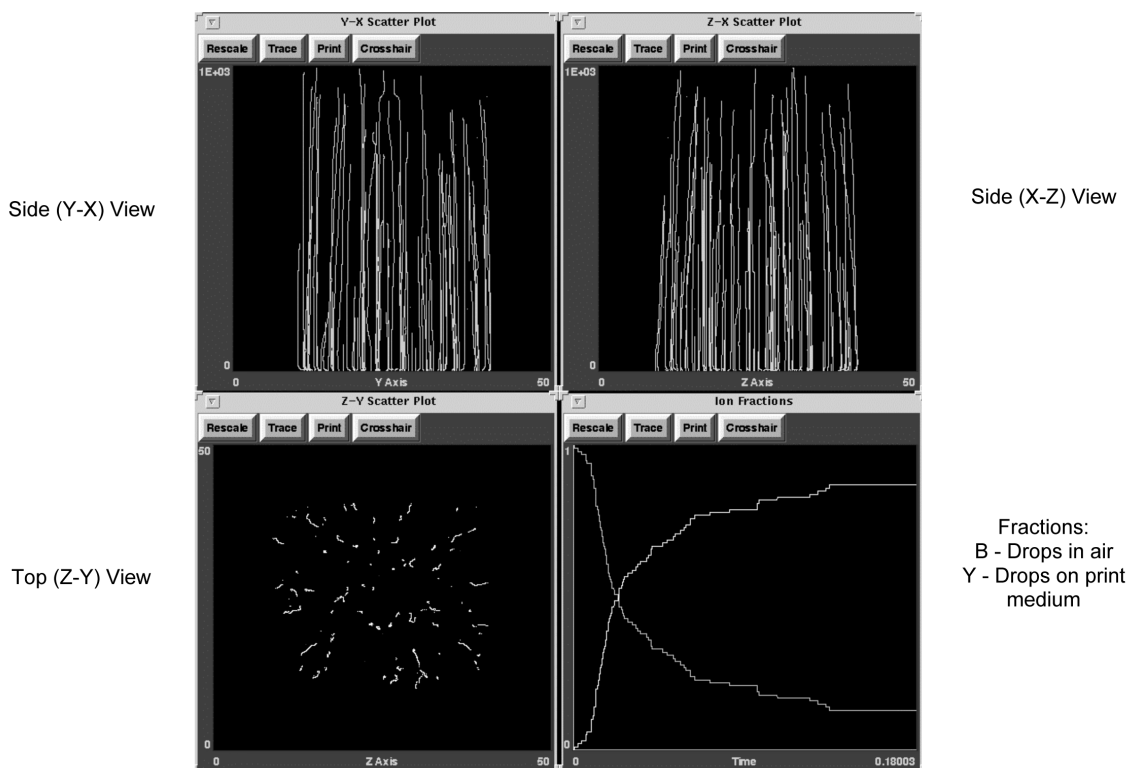|	Drift Charging Model			
Parameters	Circular Aperture		Square Aperture	
	r=15 μm		d=30 μm	
Ions on Drops	13010	54.21%	14550	60.63%
Ions on Aperture	5340	22.25%	0	0%
Ions on Collection Electrode	5650	23.54%	9450	39.37%
Total Ions	24000	100%	24000	100%
Uncharged Drops	11	11.0%	6	6.0%
Drops Outside Aperture	7	7.0%	0	0%
Charged Drops	82	82.0%	100	100%
Total Drops	100	100%	100	100%
	Sup_ion = 10, Iter = 281, Δt = 25 ns			

Figure 6. Snapshot of *Xgraphix* interactive display of dynamic droplet deposition simulation. Results are for stationary circular charging aperture and print medium using the drift attachment charging model. The top windows show side views of drop trajectories, which exhibit divergence due to mutual repulsion of ion charge. The lower left window shows the top view of the ion trajectories through a circular aperture. The lower right window shows the particle fractions for drops in air and drops deposited on the print surface. *Supplemental Materials can be found in color on the IS&T website (www.imaging.org) for a period of no less than 2 years from the date of publication.*
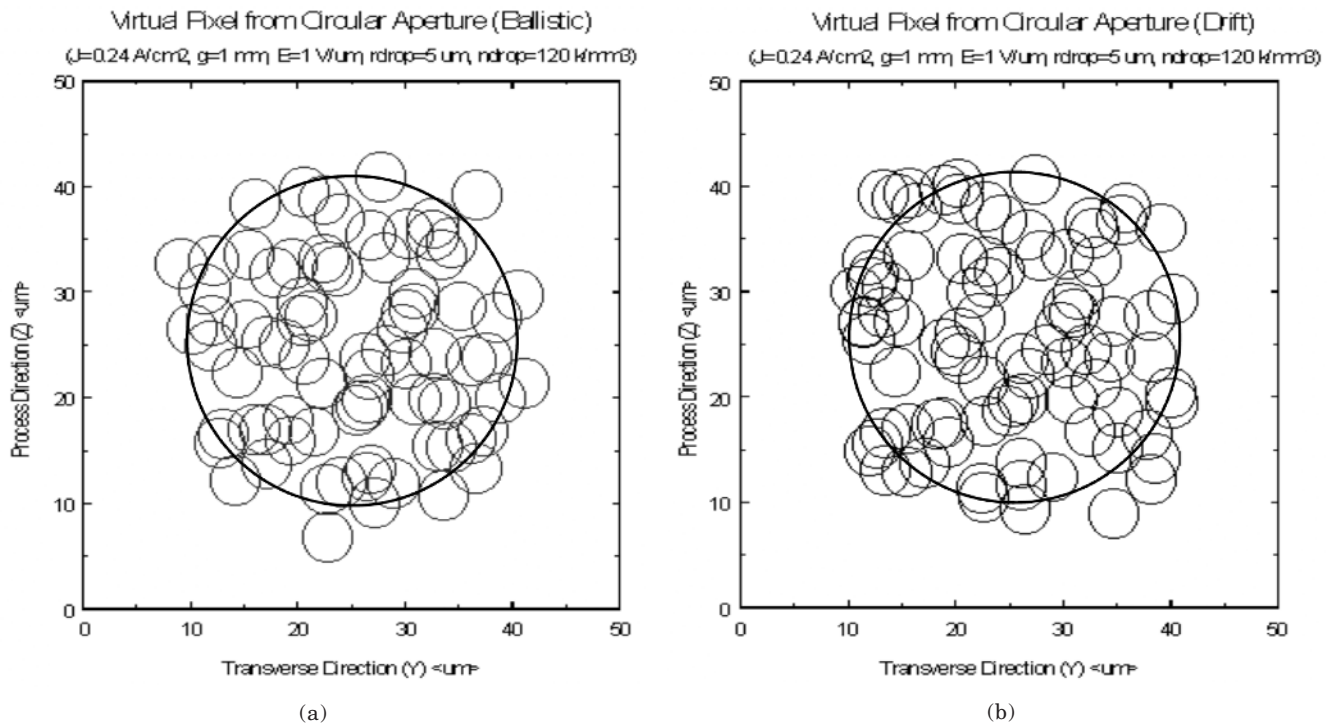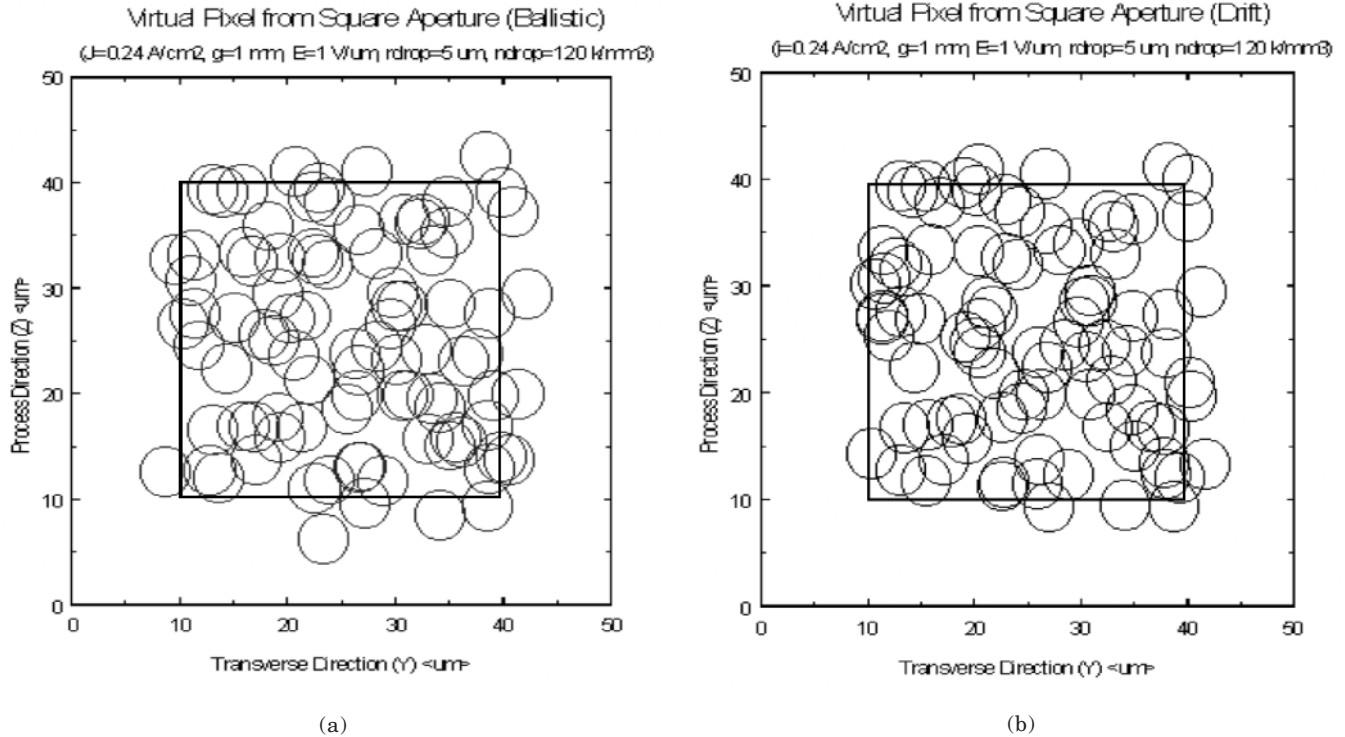
Figure 7. (a) Virtual pixel print for circular aperture with drops charged using the ballistic impact model. The original image is a 30 µm diameter circle (large circle). Smaller circles are outlines of deposited drops. Image dispersion of up to 5 µm is evident; (b) Virtual pixel print for circular aperture with drops charged using the drift attachment model. The original image is a 30 µm diameter circle. Smaller circles are outlines of deposited drops. Image dispersion of up to 5 µm is evident. *Supplemental Materials can be found in color on the IS&T website (www.imaging.org) for a period of no less than 2 years from the date of publication.*


Figure 8. (a) Virtual pixel print for square aperture with drops charged using the ballistic impact model. The original image is a 30 µm square. Small circles are outlines of deposited drops. Image dispersion of up to 5 µm is evident; (b). Virtual pixel print for square aperture with drops charged using the drift attachment model. The original image is a 30 µm square. Small circles are outlines of deposited drops. Image dispersion of up to 5 µm is evident. *Supplemental Materials can be found in color on the IS&T website (www.imaging.org) for a period of no less than 2 years from the date of publication.*
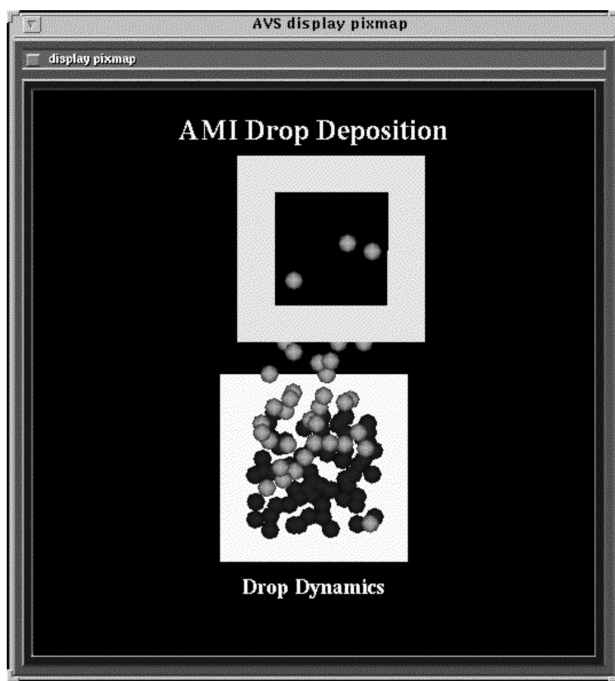
Figure 9. Perspective view of snapshot from AVS animation of drop deposition dynamics for square aperture using the drift attachment charging model showing drops in air (gray) and drops deposited on the print medium (black). This visual is for the case where both aperture and print medium are stationary. *Supplemental Materials can be found in color on the IS&T website (www.imaging.org) for a period of no less than 2 years from the date of publication.*

circular aperture case because of difference in aperture area. The general conclusion at this time is that this low level of current density does not present significant charge induced smearing.

Figure 9 shows a perspective view of a snapshot from the AVS animation of drop deposition dynamics for square aperture using the drift attachment charging model showing drops in air and drops deposited on the print medium. This visual is for the case where both aperture and print medium are stationary.

Effects of Moving Surfaces on Pixel Smearing

When the aperture and print medium moves relative to each other, the laminar airflow in the gap introduces a drag-induced image dispersion in addition to the charge-induced smearing. Results are generated for the three possible combinations and for ballistic impact and drift attachment charging models: stationary aperture with moving media, moving aperture with stationary media, and stationary aperture with stationary media.

The top graphic in Fig. 10 is a snapshot of the AVS animation for droplet deposition with moving print medium (10 ips) and stationary square aperture using the drift attachment charging model. The column of drops is stretched as the lower print medium moves to the right. The bottom graphic is the virtual pixel print with circles representing deposited drops. Clearly, there is very little lateral dispersion. However, image smearing in the process direction is about 3 mm as indicated by the extent of the red box. In fact, the image is fully deposited only about 13 mm downstream of the charging zone at 10 ips. Similarly, the top graphic in Fig. 11 is a snapshot of the AVS animation for droplet deposition
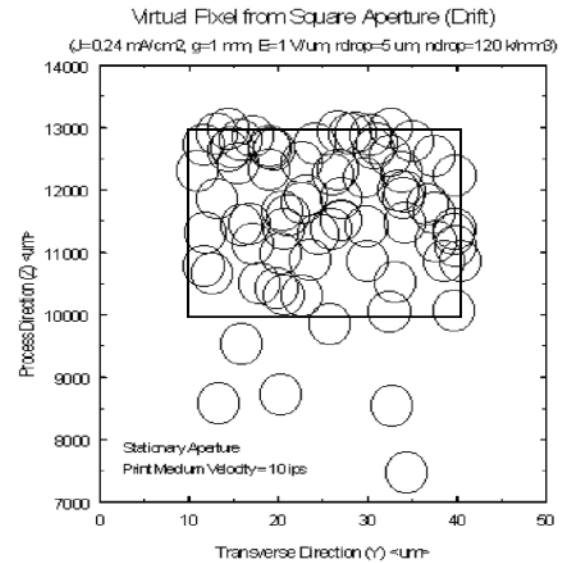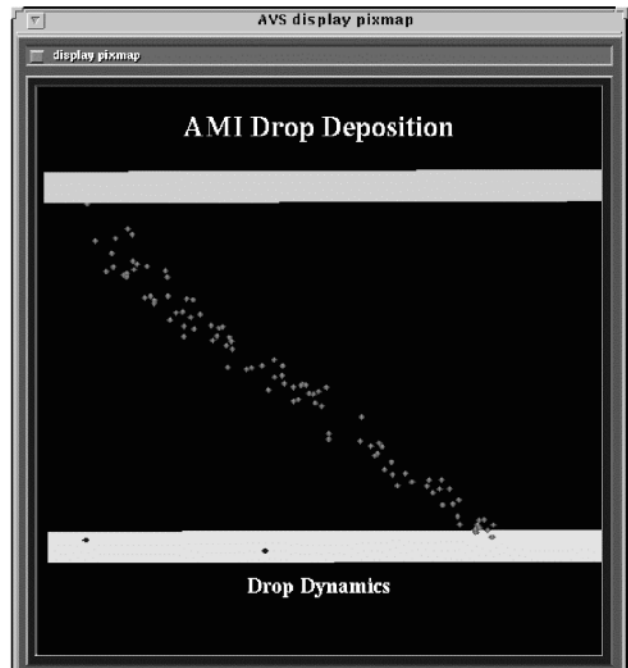

Figure 10. The top graphic is a snapshot of the AVS animation for droplet deposition with moving print medium (10 ips) and stationary square aperture using the drift attachment charging model. The bottom graphic is the virtual pixel print showing little lateral dispersion. However, image smearing in the process direction is about 3 mm. *Supplemental Materials can be found in color on the IS&T website (www.imaging.org) for a period of no less than 2 years from the date of publication.*

with synchronized moving print medium (10 ips) and moving square aperture (10 ips) using the drift attachment charging model. Because there is zero relative velocity between the two sliding surfaces, the column of drops remains intact, without being subjected to drag dispersion. The bottom graphic is the virtual pixel print showing little lateral or process direction dispersion. All the drops are deposited within 10 mm downstream of the charging zone. Finally, the top graphic in Fig. 12 shows a snapshot of the AVS animation for droplet deposition with stationary print medium and moving square
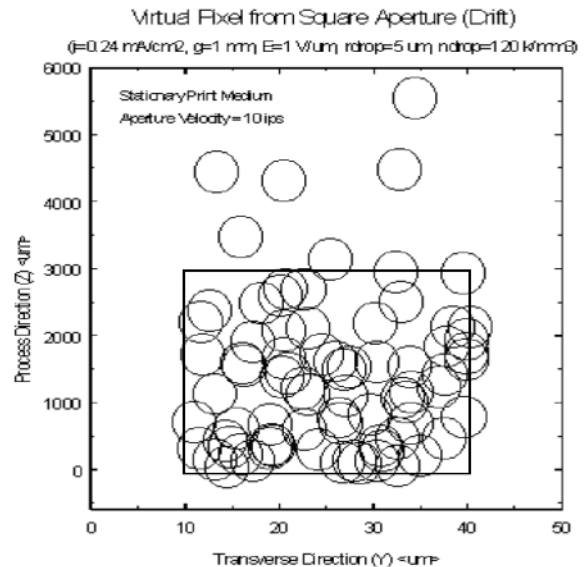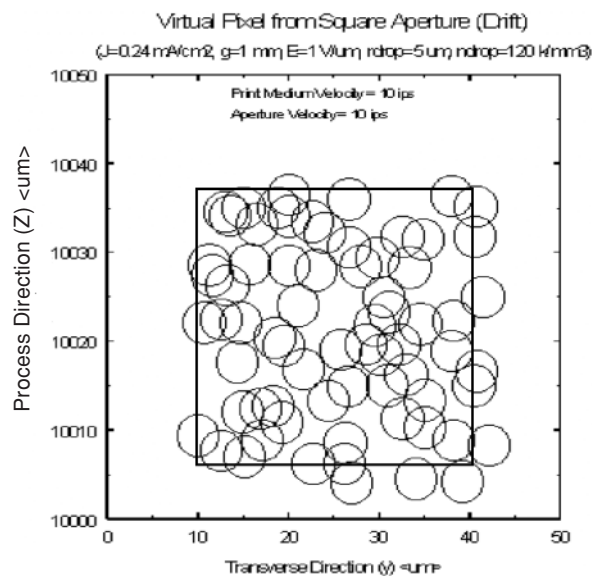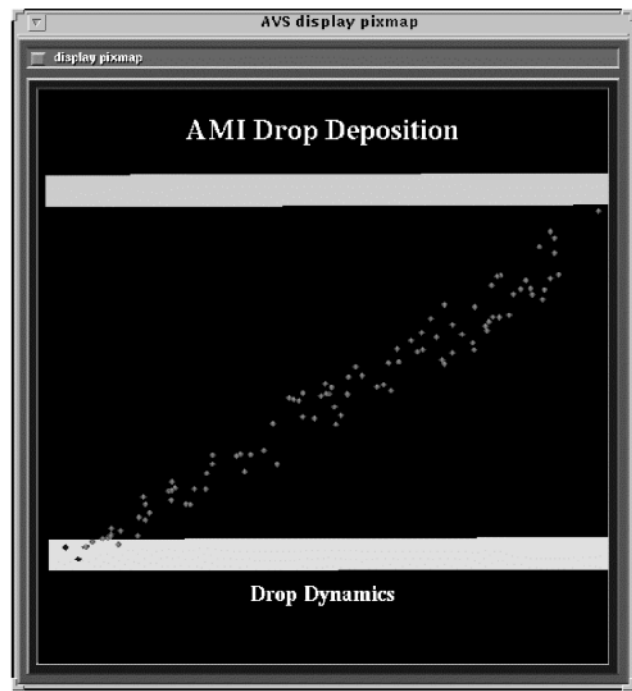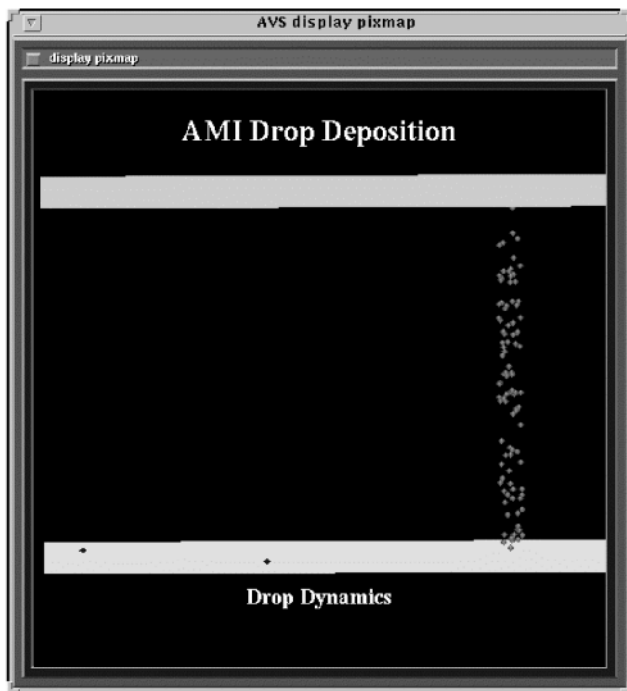
Figure 11. The top graphic is a snapshot of the AVS animation for droplet deposition with synchronized moving print medium (10 ips) and moving square aperture (10 ips) using the drift attachment charging model. The bottom graphic is the virtual pixel print showing little lateral or process direction dispersion. *Supplemental Materials can be found in color on the IS&T website (www.imaging.org) for a period of no less than 2 years from the date of publication.*

Figure 12. The top graphic is a snapshot of the AVS animation for droplet deposition with stationary print medium and moving square aperture (10 ips) using the drift attachment charging model. The bottom graphic is the virtual pixel print showing little lateral dispersion. However, image smearing in the process direction is about 3 mm. *Supplemental Materials can be found in color on the IS&T website (www.imaging.org) for a period of no less than 2 years from the date of publication.*

aperture (10 ips) using the drift attachment charging model. The column of drops is now stretched and dispersed as the upper surface has higher velocity. The bottom graphic is the virtual pixel print showing little lateral dispersion. However, image smearing in the process direction is about 3 mm. Image deposition begins almost immediately as the drops closer to the lower electrode has only a short distance to go and the flow velocity is very slow. Most of the pixel is deposited within 3

mm from the charging zone. These three sets of results indicate very clearly that drag-induced dispersion is a major concern especially at low charge, low deposition field, and high airflow velocity.

Image Smear Comparison with the EP-100 Print
As is becoming evident, two factors contribute to image dispersion in the AMI process: *excessive drop charge* and *differential drag* due to non-zero relative air gap
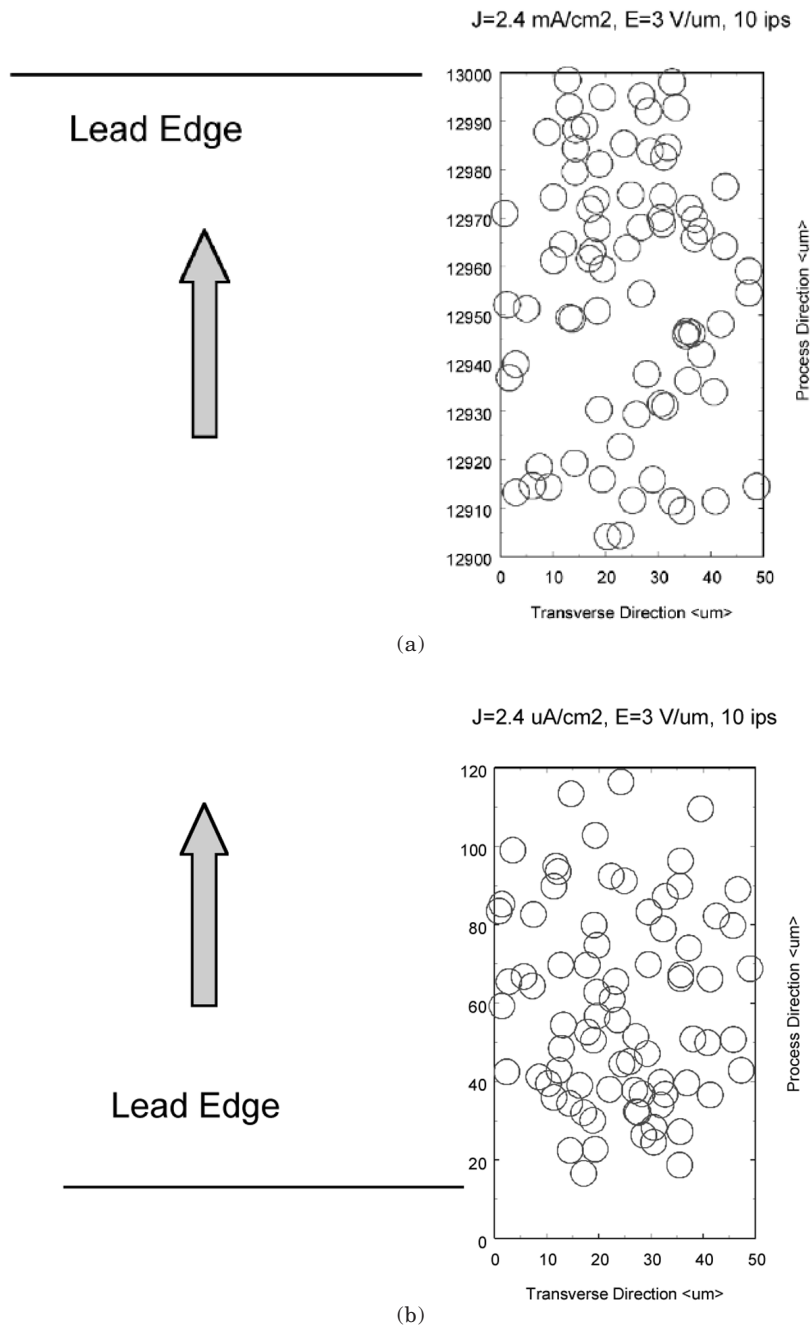
J=2.4 mA/cm2, E=3 V/um, 10 ips

Lead Edge

(a)

J=2.4 uA/cm2, E=3 V/um, 10 ips

Lead Edge

(b)

Figure 13. Virtual pixel print to compare with ElectroPrint images which do not show appreciable image smearing at 96 spi. The result here is for 600 spi with stationary aperture and moving print medium (10 ips). Charging current is increased by 10x to 2.4 mA/cm² and deposition E field is increased by 3x to 3 V/um. The resulting image dispersion is reduced from 3 mm to 100 μm, showing a linear reduction of 30x; (b) Virtual pixel print to compare with ElectroPrint images which do not show appreciable image smearing at 96 spi. The result here is for 600 spi with moving aperture (10 ips) and stationary print medium (10 ips). Charging current is increased by 10x to 2.4 mA/cm² and deposition E field is increased by 3x to 3 V/um. The resulting image dispersion is reduced from 3 mm to 100 μm, showing a linear reduction of 30x. *Supplemental Materials can be found in color on the IS&T website (www.imaging.org) for a period of no less than 2 years from the date of publication.*

velocity. Large dispersions in the process direction produce a very conspicuous image smear.

• *Excessive Drop Charge* – leads to image dispersion due to Coulomb forces that causes adjacent drops to repel each other during transit to the print medium. The printed image appears to be smeared over a larger area than the original image. Increasing the deposition E field to shorten the drop transit time can minimize this image distortion. Another important consideration is that dispersion in the transverse

direction directly limits image print resolution, although this can be relaxed by using staggered rows of lower density apertures.

• *Differential Drag* – is due to the air velocity difference in the process direction between the charging aperture and the print medium. Sample prints from the EP-100, assumed a stationary aperture and a moving print medium. As a consequence, the velocity profile begins at zero from the aperture and increases in somewhat linear fashion to reach the assigned ve-
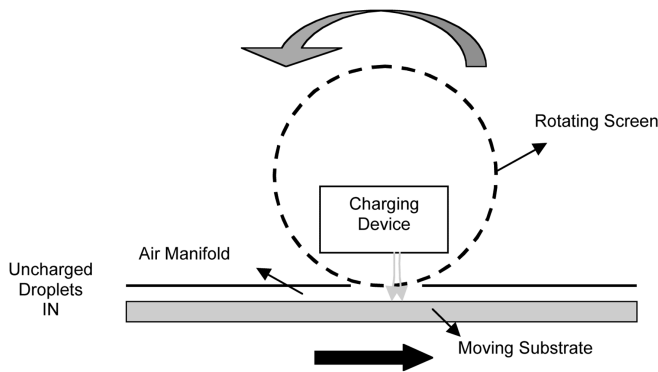
Figure 14. Cross-section of synchronized screen and substrate motion to minimize image dispersion due to non-uniform airflow in the manifold. *Supplemental Materials can be found in color on the IS&T website (www.imaging.org) for a period of no less than 2 years from the date of publication.*

locity on the print medium. Because air drag is proportional to velocity, the drag is approximately a linear function of the gap, and increases to a maximum near the print medium. This variation introduces a drag component that smears the image in the process direction. Minimizing the drop transit time in the gap can also significantly reduce this artifact.

Virtual pixel prints shown in Figs. 10 and 12 at 600 spi resolution used $J = 0.24$ mA/cm^2 and $E = 1$ V/μm resulting in a 3 mm image smear in the process direction at 10 ips. This amount of smearing is not consistent with known ElectroPrint images. By increasing the current density by 10x ($J = 2.4$ mA/cm^2), and increasing the deposition field by 3x ($E = 3$ V/μm), the corresponding pixel smear is reduced to 100 μm as shown in Fig. 13. This 30x reduction represents a linear relationship, which can be further tweaked to reproduce earlier EP-100 print process conditions. Although we can only guess at the operating conditions for the EP-100, this experiment identifies the key parameters that can be tuned to optimize print conditions. Additionally, the present resolution is 600 spi compared to the 96 spi used in the EP-100. Therefore, it is conceivable that even higher current densities may be used to result in further reduction in the amount of image smear.

Methods to Reduce Image Smearing

Any non-uniformity in the airflow across the gap is manifested as smearing of the printed image on the substrate. We consider three methods that may individually or collectively mitigate against image dispersion.

Drop Charge and Field Control

One proposal is to use a two-fold scheme to control the amount of image smearing for the case when the print head is stationary and the print medium is moving. The rationale for this idea is derived from information inferred from the model which tracks the interaction between drop charge (Q_{drop}) and the level of the deposition field (E). Design considerations for these parameters are:

• Drop charge (Q_{drop}): While larger Q_{drop} will lead to faster acceleration and shorter transit times, the mutual repulsion in transit with other drops will result in sizeable image smearing. Clearly, a compromise value exists. The preferred range of values for drop charge should be from small to moderate.
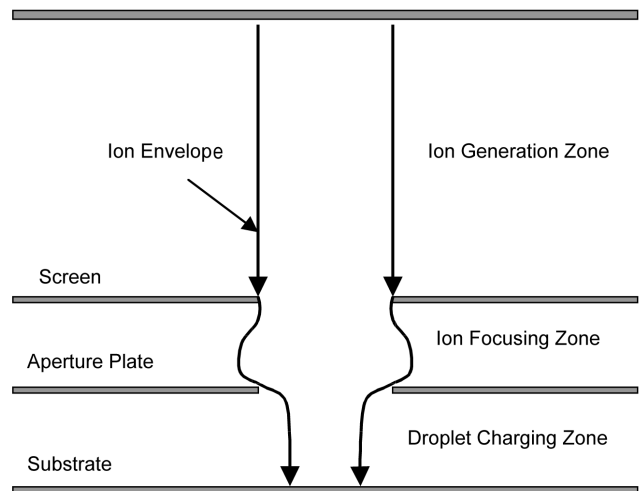

Figure 15. Cross-section of aperture plate configuration showing focusing of ion beam. *Supplemental Materials can be found in color on the IS&T website (www.imaging.org) for a period of no less than 2 years from the date of publication.*

• Deposition field (E): A larger E field produces higher drop acceleration, thus minimizing effects of transverse disturbances, including image smearing from mutual drop repulsion. However, too large an E field could lead to arcing problems.

Synchronized Aperture Motion

A second proposal is the use of a rotating apertured screen, synchronized to move in the same direction and at the same speed as the print medium. This notion is illustrated in Fig. 14. Uncharged droplets enter the air manifold from the left. A slit is opened in the top of the air manifold to accommodate an arc segment of the rotating screen, which serves to electrostatically gate ions on-demand. Droplets at the top and bottom of the manifold would then have approximately the same transverse velocity. Droplets charged within the same pixel writing burst would have little relative velocity with respect to each other, and hence suffer less relative displacement in transit.

Aperture Focusing

A third proposal is to use an electrode arrangement depicted in Fig. 15, which allows focusing of the ion beam as it propagates between the Screen and the newly introduced Aperture Plate. Without this idea, the cross-section depicted by the schematic is divided into only two zones: the Ion Generation Zone and the Droplet Charging Zone. The Screen forms the lower boundary of the Ion Generation Zone, and acts to gate ions selectively through on command in any pixel writing cycle. Given that the ion drift velocity is some 800 times faster than the droplet velocity, the charging may appear to be instantaneous with respect to the droplet. Although there is some beam divergence in transit, this effect is small and can effectively be minimized by increasing the deposition field to minimize transit time. Hence pixel size is effectively the same as the aperture dimension.

In this proposal, we insert an Aperture Plate identical to and aligned with the Screen. This plate is located halfway between the Screen and the Substrate and biased with a voltage to allow beam focusing. A new re-

Trajectory of Ion Envelope for Electrostatic Focusing

r(aperture)=25 um , gap=0.5 mm , V(top)=500, V(bottom)=-500
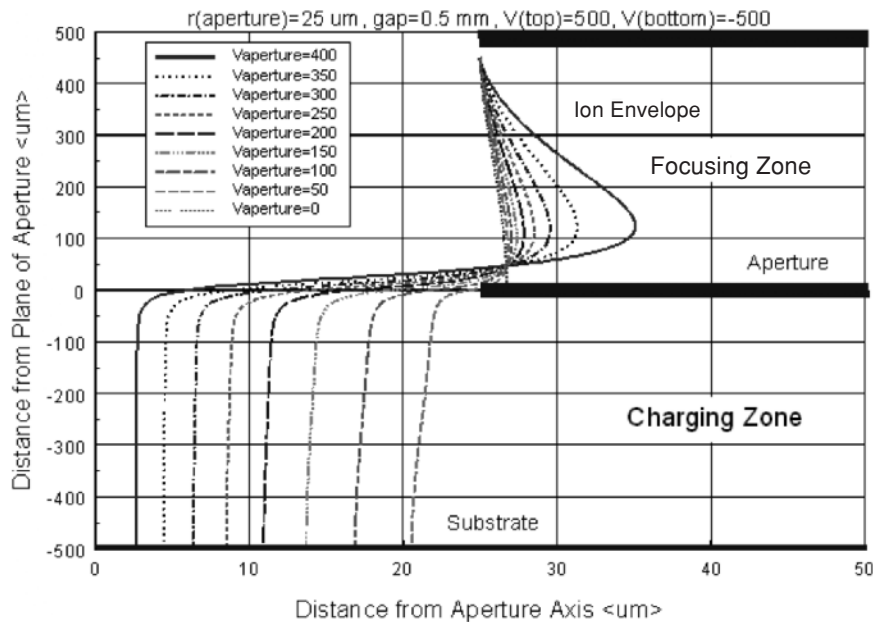
Figure 16. Computed ion beam edge for a range of Aperture Plate voltages showing focusing effect. The centerline of the ion envelopes is on the left edge. *Supplemental Materials can be found in color on the IS&T website (www.imaging.org) for a period of no less than 2 years from the date of publication.*

gion, the Ion Focusing Zone, is introduced between the two existing zones. All focusing voltages are with respect to the Screen voltage, which controls the polarity and rate of ion injection from the Ion Generation Zone into the Ion Focusing Zone. The voltage of the Aperture Plate is adjusted for the desired amount of focusing, as shown by the region within the two red curvilinear lines in Fig. 16. Zero focusing would correspond to a voltage value, which is the average of the Screen and Substrate voltages. The focussed ion beam is then used to charge droplets transiting from left to right in the Drop Charging Zone. The charged drops deposit onto the Substrate to form the image. To maintain a constant deposition field, the Substrate voltage may be allowed to float with that of the Aperture Plate.

Conclusions

Two three-dimensional particle simulation models have been developed and described in some detail. These models are used to produce prints of virtual pixels based on the AMI technology. Two drop charging schemes: ballistic impact, and drift attachment, have been implemented. Their predicted results are seen to be similar for cases with low drop density (<120,000/mm³). Collectively, the results shown in this article indicate that AMI is capable of delivering a print resolution of 600 spi at 0.24 mA/cm² and 10 ips print speed. The key problem to overcome is that of image dispersion or smearing. Factors that contribute to this image artifact are identified as excessive drop charge and differential drag. Mitigating measures have been identified and tested to compare against known ElectroPrint images. A major conclusion is that image dispersion can be fully eliminated by synchronizing the velocities of the aperture and the print medium.

While results predicted from this modeling study have yet to be experimentally verified, it has nevertheless identified a set of first-cut parameters that can be used to guide the implementation of the initial hardware prototype. Towards this end, it has served as a knowledge-based design tool to tie together several complex components to enable the printing of virtual pixels where hardware does not yet exist. As a next step, several fundamental experiments are needed to demonstrate feasibility. Key among them is the ability of the nebulizer to repeatably atomize 5 μm droplets with a narrow size distribution. These results and observations can then be fed back into the model to refine them for use in the next round of numerical experiments. These would include parametric studies to scope out the "sweet spot" for efficient device operation. ▲

References

1. *The EP-100 Line Printer*, Product literature, ElectroPrint, Inc., Cupertino, 1972.
2. How to print 8000 lines per minute, *Business Week*, October 21, 1972.
3. R.M.G. Boucher and J. Kreuter, The fundamentals of the ultrasonic atomization of medicated solutions, *Annals of Allergy*, **26,** 591 (1968).
4. M. H. Lean, J. F. O'Brien, K. Pietrowski, and H. Okuda, Microscopic particle simulation of gas ionization, *Proc. NIP-15*, IS&T, Springfield, VA, 1999.
5. W. J. Caley, W. R. Buchan and T. W. Pape, Time-resolved charge measurements on ionographic printheads, *J. Imaging Technol.* **17,** 51 (1991).
6. R. M. Schaffert, *Electrophotography*, John Wiley and Sons, New York, 1975, p.208.
7. J. L. Johnson, *Principles of Non-Impact Printing*, Palatino Press, Irvine, 1992.
8. M. H. Lean, Concurrent multi-level simulation in computational prototyping, *Int. J. Appl. E&M Mats.* **4,** 317 (1994).
9. M. H. Lean, Simulation and visualization of 3D particle cloud electrodynamics, *IEEE Trans. Mag.* **28,** 1271 (1992).
10. M. H. Lean, Particle simulations of ion cloud in a magnetic field, *IEEE Trans. Mag.* **34,** 3122 (1998).
11. R. W. Hockney and J. W. Eastwood, *Computer Simulation using Particles*, IOP Publishing, Ltd., New York, 1988.